CHAPTER 4
EXPERIMENTAL SET-UP AND CHARACTERIZATION METHODS

This chapter describes the set-up used for growing the thin films by pulsed laser (ablation)/deposition (PLD) and the various methods used in the characterization of the deposited material.

4.1 Deposition set-up

The Co-doped TiO_2 thin films were grown by PLD using the existing experimental configuration available at the Laser Surface Processing Laboratory, Department of Physics, Faculty of Science of the University of Lisbon. This configuration is based on two main equipments: a KrF excimer laser (with associated optical system) and a PLD (vacuum) chamber. A schematic view of the set-up is shown in Figure 4.1.

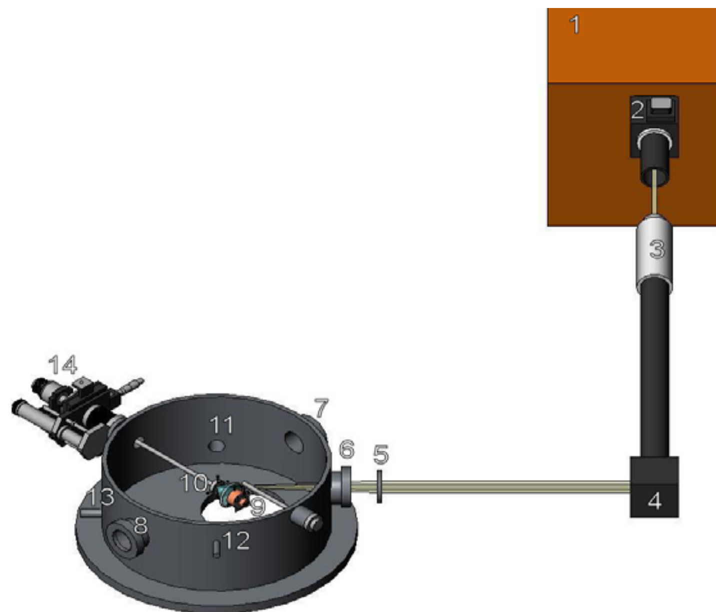

Figure 4.1 Schematic front view of the deposition set-up.

1. Excimer laser (KrF)
2. Attenuator
3. Telescope
4. Mirror
5. Focussing lens
6, 7, 8. Windows
9. Substrate holder
10. Target holder
11. Port out for the rotary pump
12. Pirani and Penning inlet
13. MKS baratron inlet
14. XYZθ motorised system

As illustrated in figure 4.1, the laser beam is deflected, focused and introduced into the vacuum chamber through a series of optical elements - mirror, focussing lens and transmission window. The laser beam is focused onto the Co-doped TiO_2 target surface, thus vaporising the material that will be deposited onto the Al_2O_3(0001) substrate. During the laser ablation/deposition pure argon or a mixture of argon and hydrogen are introduced into the chamber, the flow rates being controlled by mass flow controllers and the total pressure being measured with the aid of a baratron. Two vacuum pumps are used, a rotary vane pump during the laser processing and a cryogenic pump for attaining the base pressure before deposition.

4.1.1 The excimer laser (KrF)

A krypton fluoride (KrF) excimer laser with a wavelength of 248 nm (Lambda Physik COMPex 110) was used in the PLD experiments. An excimer[1] (short for excited dimer) is a short-lived dimeric or heterodimeric molecule formed from two species, at least one of which is in an electronic excited state. Excimers are often diatomic and are formed between two atoms or molecules that would not bond if both were in the ground state. The lifetime of an excimer is very short, of the order of nanoseconds.

The excimer molecules are formed in a gaseous mixture of the component gases of Kr, F_2 and Ne. The total pressure in the laser chamber is 3300 mbar with the partial pressure of Kr, F_2 (5% in He) and Ne being 100 mbar, 80 mbar and 3120 mbar, respectively. The ionic and electronically excited species are created by an avalanche electric discharge (~40 kV). The excited species react chemically to produce the excimer molecules, for which the ground state is repulsive and tends to dissociate rapidly. Excimers are only formed when one of the dimer components is in the excited state. When the excimer returns to the ground state, its components dissociate and often repel each other. The wavelength of an excimer's emission is longer (smaller energy) than that of the excited monomer's emission. An excimer can thus be measured by fluorescent emissions. Because excimer formation is dependent on a bimolecular interaction, it is promoted by high monomer density. Low-density conditions produce excited monomers that decay to the ground state before they interact with an unexcited monomer to form an excimer.

Commonly used excimer molecules include F_2 (fluorine, emitting at 157 nm), and noble

gas compounds, ArF [193 nm], KrCl [222 nm], KrF [248 nm], XeCl [308 nm], and XeF [351 nm].[2]

The maximum output energy of the Compex 110 KrF laser is *ca.* 350 mJ per pulse for pulse duration of 30 ns. The dimensions of the beam are ~24 × 12 mm^2 and the distribution of energy is Gaussian only in the horizontal direction or shorter axis, being top-flatted along the perpendicular axis. Figure 4.2 shows the typical beam profile of an excimer laser.

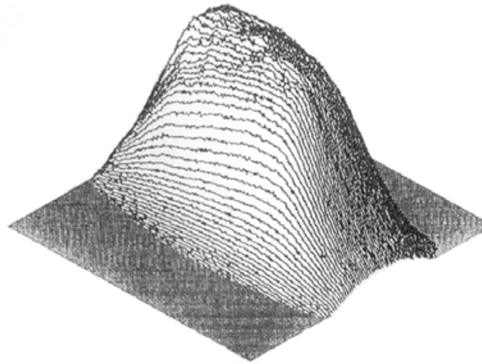

Figure 4.2 Typical beam profile (variation in intensity across the beam) for an excimer laser. Axis scales depend on the type of exciplex.

4.1.2 Optical system

A variable attenuator, Microtech UM-VAM232, mounted immediately after the exit of the beam (no. 2 in figure 4.1) was used to control the energy per pulse, and a telescope, made of a divergent and a convergent lenses, was used to collimate the beam. In fact, this element worked like a lens with a very long focal length. After this optical element a 90 degree mirror reflecting 99% of the incident radiation (at 248 nm) was used to align the laser beam with the deposition chamber/substrate.

To focus the beam on the substrate, with adequate spot size, an uncoated plano-convex lens with focal distance f = 350 mm was used. However, the actual f value at λ = 248 nm was always determined experimentally since the several optical elements used changed the beam's convergence. Prints of the beam spot on thermal paper were made as a function of the lens-image distance. The energy loss in this lens was < 5% within the energy range utilised.

The laser pulse energy was measured on a Tektronix TDS 380 (400 Mhz) oscilloscope using a Coherent J45LP energy probe (measurement given in mV). The standard deviation

of the laser pulse energy was ±10 % for the range usually used *i.e.*, 50 to 200 mV. To convert from mV to mJ we took into accout the calibration factor of the energy meter: E(mJ) = E(mV)/1.05.

During film growth, some of the evaporated material coats the entrance window, resulting in a loss of transmitted laser energy. The laser entrance window was therefore cleaned before each experiment. Since the transmission loss at the entrance view port depends on the previous use of the vacuum chamber, it is almost impossible to estimate the true laser intensity at the target surface when the laser energy is measured in front of the entrance view port, especially after evaporation of a new material. Therefore, measurement of the laser energy through the entrance window is indispensable to accurately quantify the laser energy on the target.

To calculate the energy density (or fluence) of the laser beam, the spot area on the surface of the target must also be accurately determined. Beam imprints were obtained by placing sheets of thermal paper (ZAP-IT Laser Alignment Paper) at the target position inside the chamber, and the focussing lens at 320 mm from the target surface at the focal point (the laser spot on the target has the minimum size). The spot size was determined by measuring the beam spot area on this special thermal paper from a single laser pulse at a specific path length. The area of the laser spot at its sharpest focus, A, was 2.1 ± 0.3 mm^2.

While we made no specific study of how the transmittance of the entrance view port changed during film growth, T. Ohnishi *et al.*[3] reported that the transmittance drop of the entrance view port follows Lambert's law, showing that a change in absorption, rather than reflectivity, is the dominant reason for increased loss. This behaviour is common to all PLD systems. By measuring the energy of the beam before (E_L) and after the optical component, we determined that the absorbance of the window used for transmission of the laser beam and of the focussing lens were A_w = 9.2% and A_l = 6.2% respectively, where A_w and A_l are given by:

$$A_l = \frac{E_L - E_{Ll}}{E_L} \tag{4-1}$$

$$A_w = \frac{E_L - E_{Lw}}{E_L} \tag{4-2}$$

where E_{Ll} = laser energy measured behind the lens; E_{Lw} = laser energy measured behind the window.

In these conditions, the laser fluence, F, at the surface of the target was estimated to be in the range 2.1 to 7.9 J cm^{-2}. These values were found by applying the following formula:

$$F = \frac{(1-A_l)(1-A_w)E_L}{A} \tag{4-3}$$

4.1.3 The PLD chamber

The PLD chamber consists of a stainless steel (AISI 316L) cylinder, sealed at both bases, 50 cm in diameter and 25 cm high. The chamber has 15 access openings: eight in the cylinder wall, five in the top base of the cylinder and two in its base (Figure 4.3).

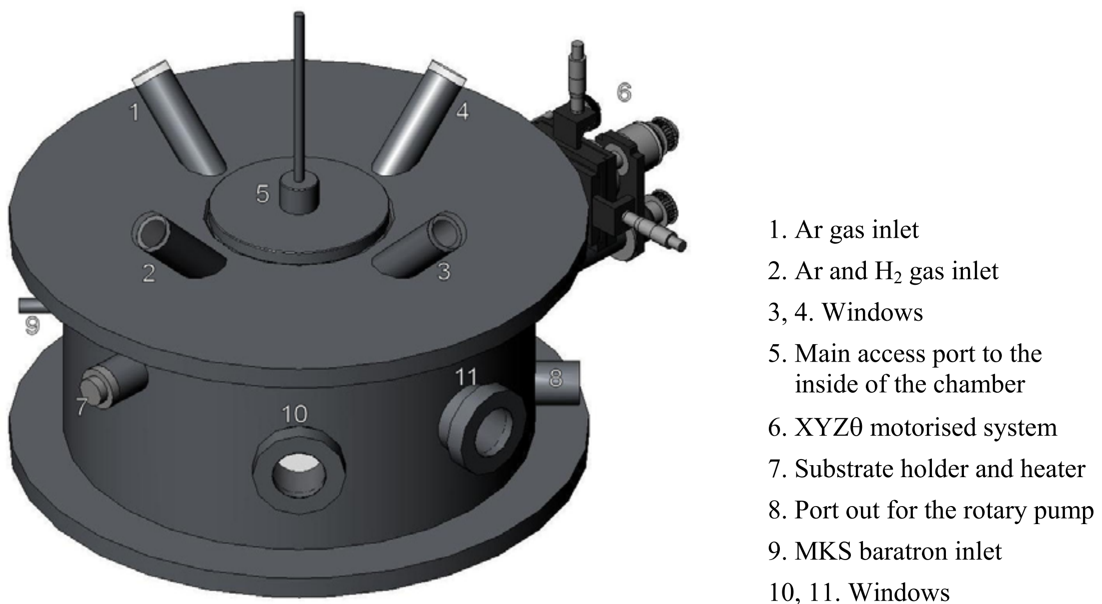

Figure 4.3 General view of the (vacuum) PLD chamber.

Figure 4.4 shows a detailed cross-section view. The eight openings in the cylinder wall permit access for the following components: one rotary vane pump (port out), one ISO Klein flange (KF10) for the pressure detection system (Pirani and Penning), one flange (KF16) for the MKS baratron, two flanges (KF40) for the target and substrate holder systems and three windows – one for the laser beam entrance and two for observation (Helma GmbG & Co. KG, 202-QS window made of Quartz Suprasil, diameter: 76.2 mm ± 0.3 mm, thickness 4 mm ± 0.1 mm, both sides with chamfer and polished). The windows are fixed with stainless steel flanges sealed with viton o’rings.

The top base of the cylinder has a central access port which permits the target and the substrate to be placed in position. Surrounding this opening there are four symmetrically distributed entrances which can have different applications, for example observation of the ablation process or the introduction of different systems such as gas pipelines. In the lower base of the cylinder there are two entrances: one for the connection to a cryopump through a gate valve sealed with a copper o'ring and the second for electrical connectors for the substrate heater.

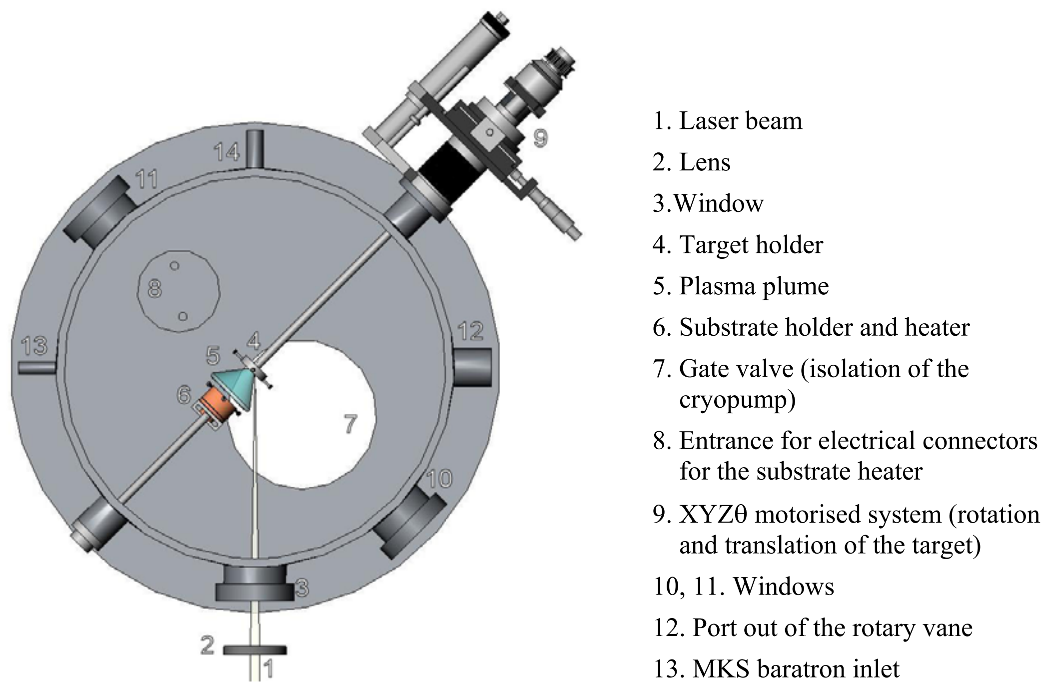

Figure 4.4 Detailed cross-section view of the vacuum chamber.

The inner surface of the vacuum chamber was electrolytically polished for reducing the rugosity, thus limiting the absorption of chemical species present in the gaseous atmosphere and possibly also preventing material corrosion.

The Al_2O_3(0001) substrates are mounted vertically inside the chamber on a copper holder containing one substrate for each experiment. The horizontal movement of the substrate holder is achieved by a metallic spindle (Edwards, 08-C006-05-00) which displaces the substrate holder laterally through the chamber.

4.1.4 Vacuum system, pressure and gas fluxes control

The film deposition takes place in a vacuum chamber held at a base pressure of around 10^{-6} mbar, which is sufficient to ensure pure films at the deposition rates used in this work. A rotary vane pump (ALCATEL PASCAL 2015 C2) with a nominal flow rate of 18 m^3/h and an APD cryopump (Air Products, Ap-8S) are used to evacuate the vacuum chamber. The ultimate pressure achieved with the rotary vane pump was 4.0×10^{-4} mbar. The cryogenic pump APD with a nominal flow rate of 4.2 m^3/h for water vapour, consisting of an HC-4 Compressor Module and a DE204SL Expander Module system, is attached to the vacuum chamber through a gate valve. The HC-4 compressor module is a single-stage, water-cooled rotary compressor designed to deliver high-pressure, oil-free helium gas to the cryogenic refrigerator. The DE204SL Expander Module is a two-stage cryogenic refrigerator using gaseous helium as the refrigerant. Power to operate the expander module is drawn from and controlled by the compressor module that supplies the required gaseous helium. The ultimate pressure inside the PLD chamber achieved with the cryopump is 4.0 $\times10^{-6}$ mbar.

A Pirani-Penning 1005 vacuum gauge is used to determine the pressure in the chamber. This model operates one Pirani head and one Penning gauge head and covers a total pressure range of 1000 to 10^{-8} mbar. The total pressure range covered by the Pirani gauge (Edwards, PRH10K) is 1000 to 10^{-3} mbar. The Pirani gauge head operates on the principle that, at low pressure, the thermal conductivity of any gas varies with pressure because the number of molecules available to transport heat diminishes as the pressure falls. The interior of the gauge head is open to the vacuum system and contains a filament that is electrically heated. The high pressure limit of the PRH10K has been extended by mounting the filament horizontally. This makes use of convection currents to transfer heat away from the filament thereby improving the high pressure sensitivity. The Penning gauge (Edwards, CP25K) operates in the range of 10^{-3} to 10^{-8} mbar. The Penning gauge head operates on the principle that, at pressures below approximately 100 mbar, the ionization current flowing between two electrodes varies with pressure. The interior of the gauge head is open to the vacuum system and contains a rod anode surrounded by a cylindrical cathode. A magnetic field is maintained in the gauge head by externally mounted permanent magnets.

An attached Baratron vacuum gauge (MKS Type 127 A) with a capacitance manometer

provides accurate, reliable and repeatable pressure measurements in the range from 1.3 bar to 0.1 mbar.

Two Mass-Flow Controllers (MKS, model M330 – 1 sccm and model 1259 C – 200 sccm) are used to introduce controlled amounts of gas into the system at fluxes between 0 and 100 sccm (standard cubic centimetre per minute). The operation is based on gas flow through a precision-manufactured sensing tube. Heat is applied to the sensor tube via two externally bound resistances, which are also used to measure heat transfer and temperature. When the molecules of the gas pass through the upstream heater, they carry a certain amount of heat. Similar heat transportation takes place through the downstream heater, but less heat is transferred because the first heater has preheated the gas. A Wheatstone bridge circuit measures the temperature difference between the two sensors. Since the difference in temperature is directly proportional to the mass flow of the gas, a highly accurate and reproducible flow measurement is obtained.

The mass flow controller (MFC) is calibrated for oxygen but can be used for any other gas provided adequate calibration is made. A carrier or reactive gas can hence be introduced in the PLD dynamic regime.

4.1.5 The temperature control system

The substrate holder (figure 4.5) consists of a cylindrical support made of copper, 40 mm in diameter and 26 mm in height, built for this purpose, and of a 90 W halogen lamp (OSRAM Halostar Starlite). The halogen lamp is positioned inside the copper cylinder (figure 4.5b) to heat the front base of the cylinder where the substrate is mounted in a cylindrical cavity (29 mm in diameter and 2 mm in thickness) and fixed with three screws.

The substrate holder can be heated from 25 °C up to 350 °C using the halogen lamp controlled by a Leybold-Heraeus Low Tension Set Transformer while a feedback system ensures a constant temperature within 2%. The temperature is measured continuously during film deposition by a K-type thermocouple fixed inside the copper cylinder and monitored by a Digital Thermometer, Thandar TH 302. The mounting of the substrate on the cylinder base ensures good thermal contact with the substrate holder.

The substrate temperature was calibrated as follows: we measured the temperature inside the copper holder and on the surface of the Al_2O_3(0001) substrate in an argon environment

(P_{Ar} = 5.0×10^{-1} mbar), using two K-type thermocouples. The calibration curve is given in figure 4.6.

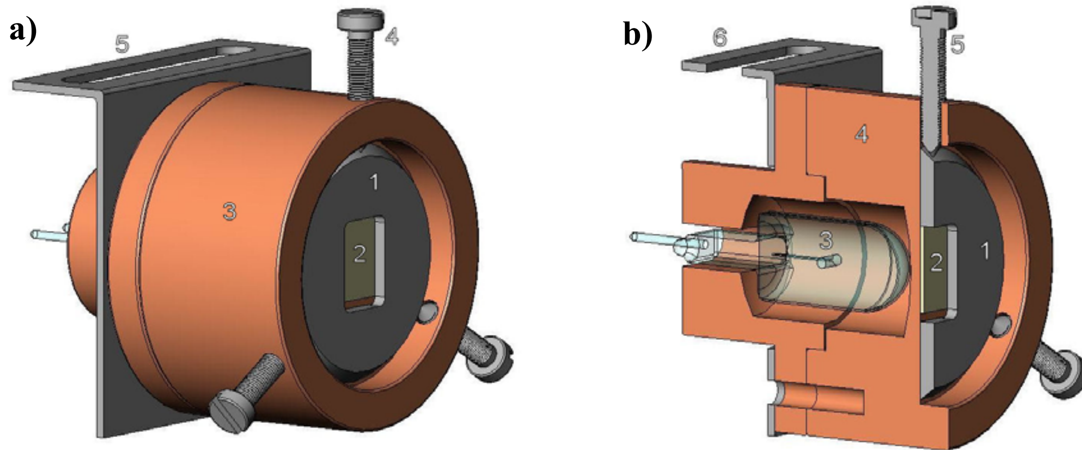

Figure 4.5 Substrate heating holder: a) Schematic side view; b) Detailed cross-section view

a)

1 - Stainless steel mask
2 - Al_2O_3 (0001) substrate
3 - Copper cylinder
4 - Screw
5 - Fixing support

b)

1 - Stainless steel mask
2 - Al_2O_3 (0001) substrate
3 - Halogen lamp
4 - Copper cylinder
5 - Screw
6 - Fixing support

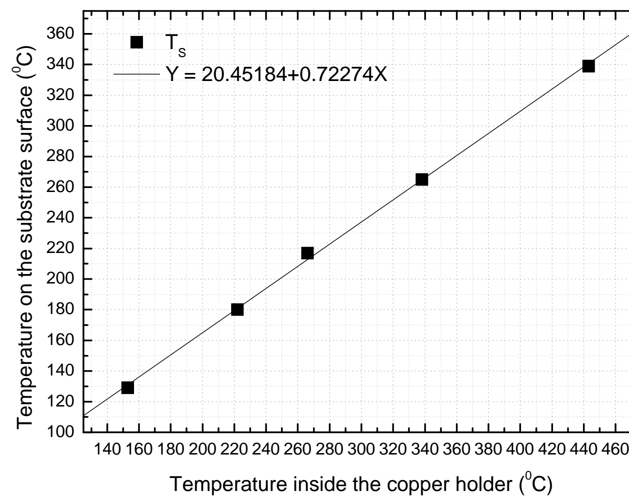

Figure 4.6 Calibration curve for Al_2O_3(0001) substrate temperature

4.1.6 The target and the substrate

Co-doped TiO_2 ceramic targets were prepared at Imperial College, London. They consist of a dry-mixture of TiO_2 rutile with 4 wt% Co_3O_4. Target purity was 99.99%. In order to remove surface impurities from the target surface and stabilise the deposition rate, targets were pre-irradiated in vacuum before each film growth series.

The target is fixed by four screws onto a cylindrical stainless steel support, 36 mm in diameter and 6 mm in depth (Figure 4.7). An appropriately programmed step-motor (ENGEL, type GNM 2145-G5) rotates the target during deposition.

Ablated target material is deposited on $Al_2O_3(0001)$ substrates placed in front of the target at 45 mm from the target surface. The substrates have the following characteristics: rectangular shape, either 10.0 mm × 10.0 mm or 10.0 mm × 5.0 mm, and a thickness of 0.5 mm.

Before initiating the deposition process, all the substrates were cleaned for five minutes in an ultrasonic bath of methanol.

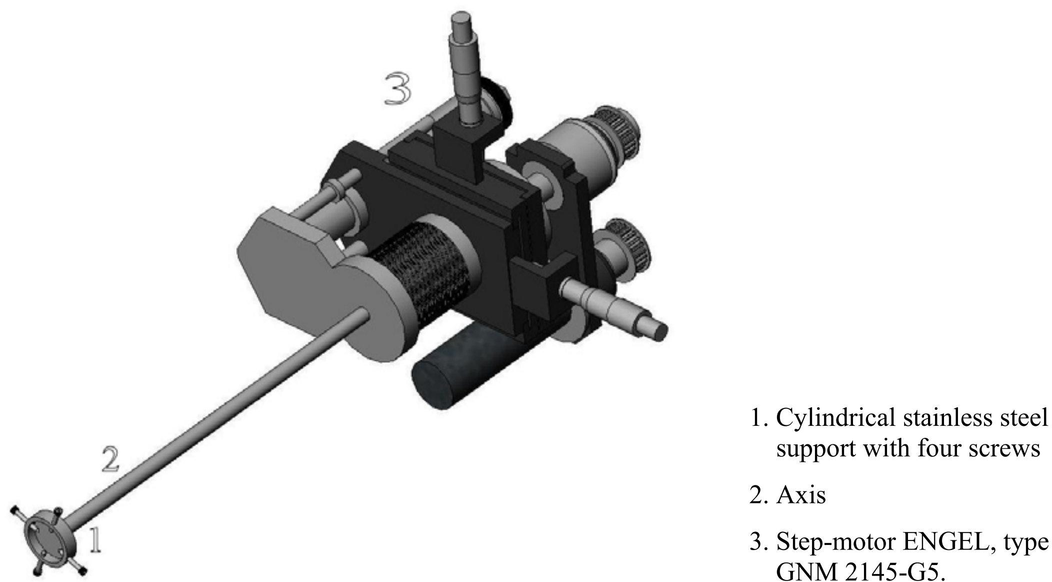

Figure 4.7 General view of the target holder.

4.2 Thin film growth parameters and procedure

4.2.1 Processing parameters

The set-up was designed to be as flexible as possible and, therefore, most of the key deposition parameters could be varied. Although these parameters are far from being independent, a comprehensive examination of all parameter variations is beyond the scope of this work. In this thesis we have focused on how film properties are influenced by the laser energy, the background gas composition and pressure and the substrate temperature. Table 4.1 summarises the film deposition parameters used throughout this work.

Table 4.1 Film deposition parameters

Parameters	**Type and/or size**	
Materials	Target	TiO_2 dry-mixed with 4wt% Co_3O_4
	Substrate	$Al_2O_3(0001)$ ≡ *c-cut* sapphire
Background gas	Ar, H_2	
Laser parameters	Wavelength	248 nm
	Repetition rate	20 Hz
	Pulse length	30 ns
	Fluence	2.1 – 7.9 J/cm^2
	Beam spot area	0.021 cm^2
Pressure parameters	Base pressure	4.0×10^{-6} mbar
	Background gas pressure	$7.0 \times 10^{-2} – 7.0 \times 10^{-1}$ mbar
Target parameters	Diameter	26 mm
	Thickness	4 mm
	Rotation frequency	3 rpm
Substrate parameters	Area	10.0 mm × 10.0 mm or 10.0 mm × 5.0 mm
	Thickness	0.5 mm
	Temperature	100 – 350 ºC

Generally, film deposition was performed in a dynamic ambient background gas, e.g. argon or argon and hydrogen, with a pressure of up to 7.0×10^{-1} mbar. The gases were let into the vacuum chamber through a completely open needle valve but their flowrates were precisely controlled. The $Al_2O_3(0001)$ substrates were heated during deposition, and subsequently cooled down to room temperature in vacuum.

4.2.2 Preparation of the samples

The film-growth experiments were carried out using the pulsed laser deposition system described above. There are five sets of experiments summarized in table 4.2. The Co-doped TiO_2 films were deposited by using a KrF excimer laser (248 nm) at a repetition rate of 20 Hz with a pulse width of 30 ns. The laser beam was introduced at an incidence angle of 45º relative to the target surface. The laser fluence at the surface of the target was estimated to be in the range 2.1 to 7.9 J cm^{-2}. To avoid local heating and drilling, the target was rotated during deposition. We used (0001) Al_2O_3 single crystals as the substrate (10 mm×10 mm×0.5 mm). The (0001) Al_2O_3 substrates were cleaned for five minutes in an ultrasonic bath of methanol before being mounted inside the vacuum chamber. The target-to-substrate distance was kept constant at 45 mm and the substrate temperature was varied between 100 and 350 ºC using an halogen lamp as heating source.

In order to remove surface contaminants, the target was irradiated with the non-focused KrF laser beam, a screen being placed between the substrate and the target for protection. The most important reason for using pre-ablation is to free the target material of loose grains which greatly affect the quality of the thin films. Another practical reason is that we want to have a constant deposition rate. Since the deposition rate decreases rapidly with time to a constant value, pre-ablation is required[4]. Also the target surface reorients itself towards the incoming laser beam[5], which causes an increase in fluence by a factor of $\sqrt{2}$ during ablation. In conclusion, pre-ablation is applied to ensure a well-defined starting situation for the actual film deposition.

Prior to deposition, the PLD chamber was evacuated to a base pressure of ~10^{-6} mbar. The typical deposition time was 50 min but some of the samples were grown thicker for various purposes. After deposition, the samples were slowly cooled down to room temperature in vacuum (10^{-6} mbar) by turning off the power at the substrate heater. For all of the experiments, a pure argon gas (99.9995% purity) and hydrogen (99.9997% purity) were provided in the deposition chamber through mass flow controllers.

Table 4.2 Film deposition parameters organized by sets of experiments.

Series of experiments	**Deposition parameters**				
	F (Jcm^{-2})	**P_T (mbar)**	**T_S (°C)**	**Φ_{Ar} (sccm)**	**Φ_{H2} (sccm)**
I	2.1-7.9	5.0×10^{-1}	250	30	–
	2.1-6.4		310		
II	6.4	7.0×10^{-2} – – 7.0×10^{-1}	310	30	–
	7.9	2.5×10^{-1} 5.0×10^{-1} 7.5×10^{-1}	250		
III	5.1	5.0×10^{-1}	100 200 250 310	180	1
	6.4		200 250 310 350	30	–
IV	5.1	5.0×10^{-1}	310	6 30 180 270	–
		7.0×10^{-2}		6 30	
V	6.4	1.0×10^{-1}	310	30	0 0.04 0.1 0.2 1
			200		0.1 0.2 0.5 1

4.3 Characterization methods

In order to study the influence of the deposition parameters on the properties of the deposited films, the latter were analysed by several techniques allowing to carry out structural, morphological, chemical, optical, electrical and magnetic characterization. In particular, the following methods were used: X-ray Diffraction (XRD), Field Emission Gun − Scanning Electron Microscopy (FEG-SEM), Atomic Force Microscopy (AFM), X-ray Photoelectron Spectroscopy (XPS), Rutherford Backscatering Spectrometry (RBS), Optical Absorption/Transmission, resistivity measurements by the Four Points technique and magnetization measurements. The RBS analyses were performed at Instituto Tecnológico e Nuclear (with Dr. R.C. da Silva) and the XPS ones at Instituto Superior Técnico (with Prof. A.M.B. Rego). The magnetic studies were conducted at Imperial College, London, UK, by Prof. L.F. Cohen's group using a vibrating sample magnetometer (VSM) and also at FCUL, in a SQUID, by Prof. M.M. Cruz. A few samples were investigated by spectroscopic ellipsometry at FCTUNL (with Dr. H. Águas).

A brief introduction to these techniques is given below, followed by a short description of the equipment and parameters used.

4.3.1 X-ray Diffraction (XRD)

X-ray diffraction techniques are the principal source of information about the crystallographic structure of materials, despite the complementary information allowed by electron and neutron diffraction. Typical interatomic distances in a crystalline solid are of the order of one ängstrom (10^{-8} cm). An electromagnetic probe of the microscopic structure of a solid must therefore have a wavelength close to this short value, corresponding to an energy value of $h\upsilon = hc/\lambda = hc/10^{-8}\ cm \approx 12.3\times10^{3}\ eV$. Energy values like this one are characteristic of X-rays (1 keV − 120 keV). Therefore, a crystal may be seen as a three-dimensional diffraction grating for such electromagnetic radiation. W.L. Bragg accounted for this by regarding a crystal as made out of parallel planes of atoms, spaced a distance d apart (lattice planes). The conditions for a sharp peak in the intensity of the scattered radiation are the following:

i) the X-rays should be specularly reflected by the ions in one plane, and

ii) the reflected X-rays from successive planes should interfere constructively.

X-rays specularly reflected from adjoining planes are schematically shown in figure 4.8.

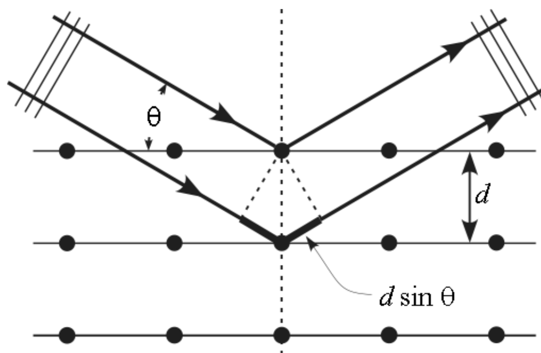

Figure 4.8: A Bragg reflection from a particular family of lattice planes, separated by a distance *d*. Incident and reflected rays are shown for two neighbouring planes. The path difference is 2 d_{hkl} sin θ.

The path difference between the two rays is just 2 $d_{hkl} \sin\theta$, where θ is the angle of incidence[(a)]. For the rays to interfere constructively, this path difference must be an integral number of wavelengths, leading to the well known Bragg law,

$$2\, d_{hkl} \sin\theta = n\,\lambda \qquad (4\text{-}4)$$

where *n* defines the order of the reflection.

Modern X-ray crystal analysis is usually done with X-ray diffractometers. A diffractometer has a radiation counter (detector) to detect the angle and the intensity of the diffracted beam. In particular, when using Bragg-Brentano or θ-2θ configuration the detector is rotated at a double angular speed as the sample.

A recorder automatically plots the intensity of the diffracted beam as the counter moves on a goniometer circle which is in synchronization with the specimen over a range of 2θ values. In this way, both the angle of the diffracted beam and the intensity can be recorded at one time. An X-ray diffraction pattern is thus a plot of the intensity of the diffracted beam *vs.* the diffraction 2θ angle, the peak intensities and their 2θ angular positions giving information about the crystallographic structure of the material; the 2θ angular positions are related to certain lattice plane distances d_{hkl} and thus to certain lattice planes (*hkl*).

Bragg's law states the condition for a sharp-diffraction peak (Fig. 4.9a) from an infinite crystal with a perfect 3D order. Typically, the diffraction peak has a finite width which is induced either by instrumental broadening (due to non ideal X-ray optics, wavelength

[(a)] The angle of incidence in X-ray crystallography is conventionally measured from the plane of reflection rather than from the normal to that plane, as in classical optics. It should be noted that θ is just half the angle of deflection of the incident beam, which is 2θ.

dispersion, sample transparency, axial divergence, flat sample effect, and detector resolution) or with deviations from ideal crystallinity such as finite crystallite size, extended defects (stacking faults and antiphase boundaries) and lattice strain (microstrain). By analyzing this broadening it is possible to extract information about the microstructure of a material, in particular the average crystallite size can be inferred using the Scherrer equation[6]:

$$<t> = \frac{K\lambda}{B\ \cos\theta_{hkl}} \tag{4-5}$$

where $< t >$ stands for the average crystallite size, K is a constant whose value depends on the shape(s) of the crystallites (typically K has a value between 1 and 0.9) and B is the peak breadth (in radians $2\theta_{hkl}$) centred at the Bragg angle θ_{hkl} corresponding to the (*hkl*) reflection (see Fig. 4.9b). It is worth noting here that crystallite size should not be confused with particle size which can be associated with the presence of polycrystalline aggregates.

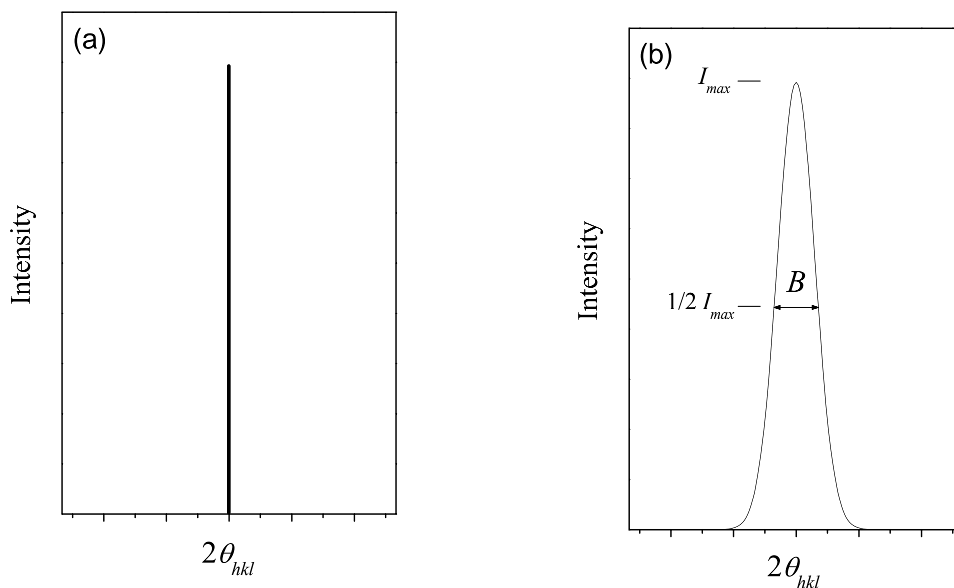

Figure 4.9 Effect of fine crystallite size on diffraction lines. a) (hkl) diffraction peak from an infinite crystal with a perfect 3D order (hypothetical case); b) peak broadening due to small crystallite size.

Our samples were examined using a Siemens D5000 diffractometer and Cu K_{α} radiation (λ=0.15418 nm) at 40 KV and 30 mA in θ–2θ coupled mode (Bragg-Brentano configuration)[7]. The diffraction patterns were recorded in the range of 18º - 60º with a step size of 0.02º and a time per step of 15 seconds. While recording XRD spectra, the samples

were rotated to homogenize the measurements. All the recorded spectra were compared with the standard files from the "Joint Committee of Powder Diffraction Standard" (JCPDS)[8]. Figure 4.10 shows the XRD pattern of the target used to grow the Co-doped TiO_2 thin films and table 4.3 collects the 2θ angular positions and the relative intensities for the (*hkl*) diffraction planes of both rutile and anatase TiO_2 phases.

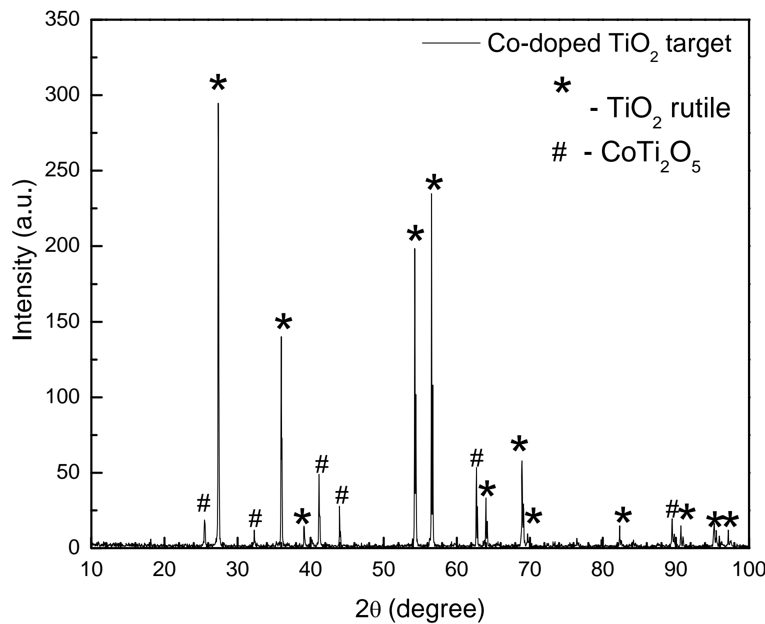

Figure 4.10 XRD pattern of the Co-doped TiO_2 target used for the deposition of the films.

Table 4.3 Position and relative intensity of the diffraction lines originating from the (hkl) planes of TiO_2 rutile and TiO_2 anatase according to the JCPDS database cards no. 21-1276 and 21-1272, respectively.

TiO_2 rutile			TiO_2 anatase		
2θ	I	hkl	2θ	I	hkl
27.447	100	110	25.281	100	101
36.086	50	101	36.947	10	103
39.188	8	200	37.801	20	004
41.226	25	111	38.576	10	112
44.052	10	210	48.050	35	200
54.323	60	211	53.891	20	105
56.642	20	220	55.062	20	211
62.742	10	002	62.121	4	213
64.040	10	310	62.690	14	204
65.480	2	221	68.762	6	116
69.010	20	301	70.311	6	220
69.790	12	112	74.031	2	107
72.410	2	311	75.032	10	215
74.411	1	320	76.020	4	301
76.510	4	202	80.727	2	008

4.3.2 Field Emission Scanning Electron Microscopy (FEG-SEM)

A scanning electron microscope (SEM) produces images of the surface of a sample by scanning it with a high-energy electron beam; the electrons are thermionically emitted from a tungsten or lanthanum hexaboride (LaB_6) cathode. The interaction of the electron beam with the near-surface region of the specimen generates secondary electrons (SE), back scattered electrons (BSE), characteristic X-rays and light (cathodoluminescence)[9]. SE imaging is the SEM primary detection mode. In this mode, a SEM can produce high-resolution images, the large depth of focus yielding a characteristic three-dimensional appearance useful for understanding the surface structure of a sample. Besides SE image mode, also back-scattered electrons may be used to form an image. BSE imaging is usually applied to detect contrast between areas with different chemical composition, especially when the average atomic weight of the various phases are different since the electron yield in BSE image increases with the atomic weight.

Instead of a thermionic cathode, the use of a field-emission cathode in the electron gun of a scanning electron microscope provides narrower probing beams at low as well as high electron energy, resulting in improved spatial resolution. Field-emission gun scanning electron microscopes (FEG-SEM)[9] are similar to SEM equipments but with several advantages, e.g.:

- they produce clearer, less electrostatically distorted images with spatial resolution down to 1.5 nm (3 to 6 times better than conventional SEM);
- they allow to obtain high quality images at lower accelerating voltages, thus with negligible electrical charging and damage of the samples;
- the need for placing conducting coatings on insulating materials is virtually eliminated.

The electron microscope images showed in this thesis were obtained using an analytical FEG-SEM JEOL 7001F. The samples were not coated with any conducting film and because of this low voltage values were usually used.

4.3.3 Atomic Force Microscopy (AFM)

The Atomic Force Microscope (AFM) is a type of scanning probe microscope whose central component is a micron-sized cantilever with a sharp tip (probe) that is used to scan

the specimen surface. The cantilever is affected by the interactions between the tip and the atoms of the sample’s surface, e.g. mechanical contact forces, Van der Waals forces, capillary forces, electrostatic forces, magnetic forces, Casimir forces, and so on. These interactions lead to a deflection of the cantilever according to Hooke's law. The cantilever’s deflection is usually measured by using a laser beam reflected from the top surface of the cantilever into an array of photodiodes. An AFM can be operated in tapping, contact and non-contact scanning modes, depending on the application[10].

The AFM has several advantages over electron microscopy techniques, namely the AFM provides a true three-dimensional surface profile while for an electron microscope a two-dimensional projection or a two-dimensional image of a sample is obtained. Moreover, an AFM can be run perfectly well in ambient air, and samples do not require any special treatment that would irreversibly damaged them. Typical AFM values for the depth resolution and lateral resolution (probe size) are 0.01 nm and 1 - 1.5 nm, respectively, enabling near atomic resolution imaging analyses. The AFM is thus a very suitable technique for thin film surface analysis, including roughness and grain size measurements.

A Digital Instruments™ microscope was used in this work, and the thin film surfaces were always scanned in the tapping mode.

4.3.4 X-ray Photoelectron Spectroscopy (XPS)

XPS (X-ray Photoelectron Spectroscopy) or ESCA (Electron Spectroscopy for Chemical Analysis) has been widely used as a surface analysis technique due to its high information content, flexibility in addressing a wide variety of samples and sound theoretical basis[11].

Over the past few decades, XPS has been developed as a key surface characterization method which combines surface sensitivity with the ability to quantitatively obtain both elemental and chemical state information. Data interpretation has been established using a number of published databases[12] and in recent years, on-line services have become available over the Internet[13]. As it is well known, XPS is now a very important analytical tool in the area of thin films[11]. XPS analysis provides valuable information about the composition, chemical state, thickness, etc. of thin films.

XPS is based on the photoelectric effect outlined by Einstein in 1905 where the concept of the photon was used to describe the ejection of electrons from a surface when photons

impinge upon it. This process can be expressed by the following equation:

$$\mathrm{BE} = h\nu - \mathrm{KE} - \mathrm{f} \tag{4-6}$$

where BE is the binding energy of the electron in the atom (a function of the type of atom and its environment), $h\nu$ is the photon energy of the X-ray source, KE is the kinetic energy of the emitted electron that is measured in the XPS spectrometer and f is the spectrometer work function. For XPS, Al Kα (1486.6 eV) or Mg Kα (1253.6 eV) are often the photon energies of choice. Other X-ray lines can also be chosen, such as Ti Kα (2040 eV).

The XPS technique is highly surface-specific due to the short range of the photoelectrons that are excited from the solid. The energy of the photoelectrons leaving the sample is determined using an analyzer and this gives a spectrum with a series of photoelectron peaks. The binding energy of the peaks is characteristic of each element. The peak areas can be used, with appropriate sensitivity factors, to determine the composition of the materials surface.

The shape of each peak and the binding energy can be slightly altered by the chemical state of the emitting atom. Hence XPS can provide chemical bonding information as well. XPS is not sensitive to hydrogen or helium, but can detect all other elements. Normally, in the outmost 10 nm of thin-film surfaces, XPS can identify all elements (present at concentration > 0.1 at. %) except for H and He.[14] The analysis of composition has been widely applied in thin-film research − the composition of thin films can be determined from XPS spectra. The information of all elements in a thin film can be gained from the survey scan spectrum of XPS, whereas detailed information of each element can be obtained from the narrow scan spectrum. Wide scan spectra give information on elements in thin films and contaminants adsorbed on the thin films.

4.3.5 Rutherford Backscattering Spectrometry (RBS)

Rutherford Backscattering Spectrometry (RBS) is a powerful analytical technique, nowadays well established as one of the principal methods for quantitative analysis of materials composition and depth profiling in the near surface region of solids[15]. In an RBS experiment the solid material to analyse (the target) is bombarded by a particle beam, typically $^1H^+$ or $^4He^+$ ions, with energies in the range of 0.4 − 2 MeV. Detection of the

scattered particles is done for scattering angles larger than 90º, the energy spectra holding information about the target composition and the in-depth distribution of the constituent elements.

The physical quantities and concepts that enable one to analyze the RBS spectra are the same that characterize the interactions between beam ions and target atoms:

- kinematic factor, K: it allows mass analysis, i.e. the identification of the constituent elements in the target, through the conversion of features in the energy spectra in mass spectra;
- scattering cross-section, σ: it allows a quantitative analysis of composition, by establishing a correspondence between spectral intensities and the density of the corresponding scattering nuclei;
- target stopping power, S: it allows depth analysis, i.e. the conversion of energy intervals in the spectra to depths – the energy scale thus become a depth scale – for each element in the target material;
- energy straggling: the fluctuations in the energy losses of the incoming ions through the target, or straggling, limits the possible depth resolution.

The scattering cross-section and stopping power concepts give the technique the unique ability of converting a spectrum in a depth profile, i.e. in a concentration vs. depth curve, for each element identified in the spectrum by its kinematic factor.[15]

As an example, Fig. 4.11 shows the RBS spectrum from a thin film deposited on a substrate. The energy width of the particles scattered at the front and back surfaces of the film is related to the number (*Nd*) of atoms per unit area of the film through the following equation[16]:

$$\Delta E = [\varepsilon_0]Nd \qquad (4\text{-}7)$$

where $[\varepsilon_0]$ is the surface approximation for the stopping cross section factor, N is the atomic density and d the thickness of the film.

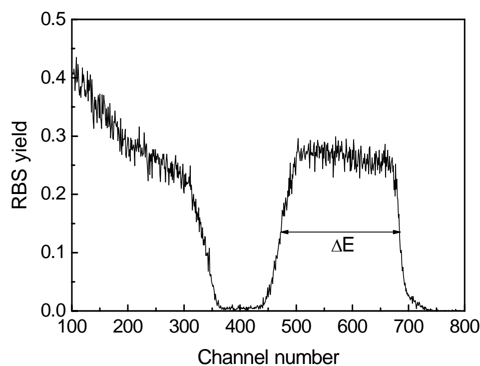

Figure 4.11 RBS spectrum from a thin film on a substrate.

Some of the Co-doped TiO_2 films were characterized using RBS in order to determine the thickness and the chemical composition of the samples. These measurements were performed using a 1 mm collimated 2 MeV ^{4}He beam, with the samples mounted in a computer controlled two-axis goniometer with an accuracy of 0.01º. The projectiles hit the sample under normal incidence. Two surface barrier silicon detectors, placed at 140º and close to 180º with respect to the beam direction, and with energy resolution of 13 and 16 keV, respectively, were used to detect the backscattered particles. The depth profiles of the elements were extracted from the data using a simulation program (RUMP, developed by L.R. Doolittle[17].

4.3.6 Optical transmission/absorption measurements

The characterization of thin films can be extremely challenging for mainstream metrology tools such as ellipsometers, interferometers and profilometers. One promising method is broadband spectrophotometry: if applied in conjunction with an appropriate physical model for data analysis, it can provide important information about thin-film thickness and optical properties in a single, non-destructive step.

Optical characterization of thin films involves the determination of film thickness, d, complex index of refraction, $\boldsymbol{n}$, and absorption coefficient, α. Another useful parameter is the film's energy band gap, E_{gap}, which represents the minimum photon energy needed for a direct electronic transition from a valence band to a conduction band. The measurement of the absorption coefficient for various energies gives information about the band gaps of the material. Knowledge of these band gaps is extremely important for understanding the electrical properties of a semiconductor, and is therefore of great practical interest.

Thus, optical analysis provides a good way of examining the properties of semiconductors and is usually the preferred method for measuring thin films because it is accurate, non-destructive, and requires little or no sample preparation. We used the transmission/absorption spectrophotometry technique to investigate our Co-doped TiO_2 thin films.

For transmission/absorption spectrophotometry we used a commercial spectrophotometer (SHIMADZU, model UV-1603) allowing to record spectra in the UV-VIS-NIR range, from 200 to 1100 nm. In practice, the transmission/absorption measurements are limited to

wavelengths at which samples have medium absorption coefficients. For high absorption there is virtually no transmission. However, if α is too low, thin-film interference effects will appear because light waves that are reflected on the two sides of the film will be superimposed on one another.[18-21]

In the following, a short description is given of the architecture of the optical system and of the general principles governing its function. To compensate for the complicated intensity distribution of the light source, the spectrophotometer does not measure absolute values but instead the signal from the sample is compared to a reference beam. Additionally, a baseline is recorded prior to the measurements to calibrate the instrument.

Optical system − description of layout and general principle of functioning

The figure below shows the architecture of the optical system and the general principle of functioning of the spectrophotometer used in our studies.

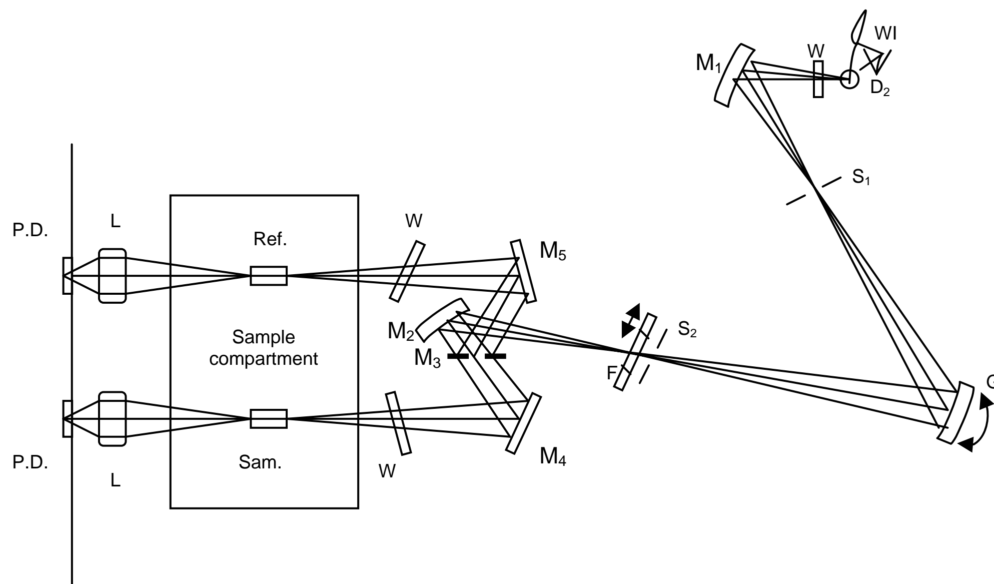

Figure 4.12 Scheme of the optical path and components of the Shimadzu UV-Visible Spectrophotometer. D_2: deuterium lamp; WI: halogen lamp; W: window plate; M_1 – M_5: mirrors (M_3 is a half-mirror); S_1/S_2: entrance/exit slits; G: grating; F: filter; Sam.: sample cell; Ref.: reference cell; L: lens; P.D.: photodiode.

The light beam emitted from the light source (deuterium lamp, D_2, or halogen lamp, WI) is reflected by the mirror M_1, and directed into the monochromator. The light sources are interchanged automatically according to the wavelength range as follows:

− D_2 lamp: from 200 nm to the light-source-switching wavelength, minus 0.1 nm.

− WI lamp: from the light-source-switching wavelength to 1100 nm.

− The light-source-switching wavelength can be set to any value within the range of 295 nm to 364 nm. Its initial value is 350.5 nm.

The light source position is automatically controlled for maximum sensitivity and the light source condensed mirror is located outside the light source housing so as not to be exposed to heat rays and ozone. All the optical elements, excluding the light source, are isolated from the external atmosphere by sealed window plates, W, in order to stay dust free.

The slit width of the monochromator is fixed at 2 nm. The grating is a Shimadzu-made 900 lines/mm aberration-corrected concave holographic grating. The light beam coming from the monochromator is passed through the stray-light cut-off filter, F, reflected by the mirror M_2, and then split by the half mirror M_3 into the sample and the reference beams. Each beam passes through the respective cell to the detector (Si photodiode). In this way, the complex intensity distribution of the light source is avoided since the signal originating from the sample is compared with the reference beam.

An image of the exit slit S_2 appears near the cell position in the sample compartment. Its cross-sectional size is ~1.2 mm large and ~16 mm high.

Because the size of our samples are not always constant and the thickness of the films can vary from the center to the periphery, a special sample holder with mask was designed to ensure a constant beam spot size impinging on an uniform portion of the sample. Also, in our case the reference cell was replaced by a pristine substrate.

Determination of the refractive index

Besides providing information about the absorption of the sample, transmission spectra can give important information about its refractive index.

The complex refractive index, **n**, of a thin film can be calculated from the transmittance spectrum using the Swanepoel method[22]. This method can be applied to thin films deposited on transparent substrates several orders of magnitude thicker than the film. A practical situation is shown in figure 4.Figure 4.13, where d and n are the thickness and the refractive index of the film respectively, k is the extinction coefficient ($\mathbf{n}=n-ik$), α the absorption coefficient, n_s the refractive index of the substrate, and α_s the absorption coefficient of the substrate. The index of the surrounding air is $n_0=1$.

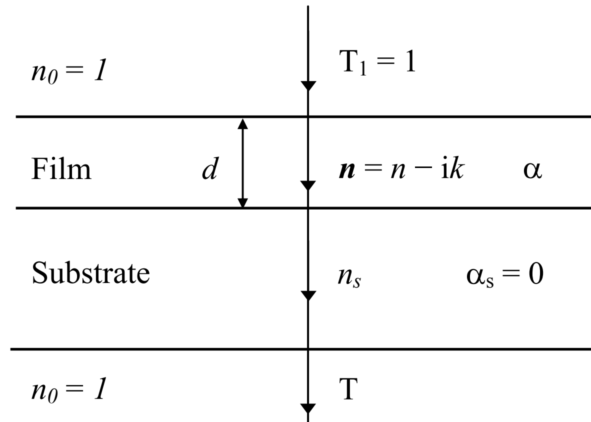

Figure 4.13 An absorbing thin film on a thick, finite, transparent substrate.

When film thickness is uniform, interference effects give rise to the typical transmittance spectrum with successive maxima and minima shown in figure 4.14.

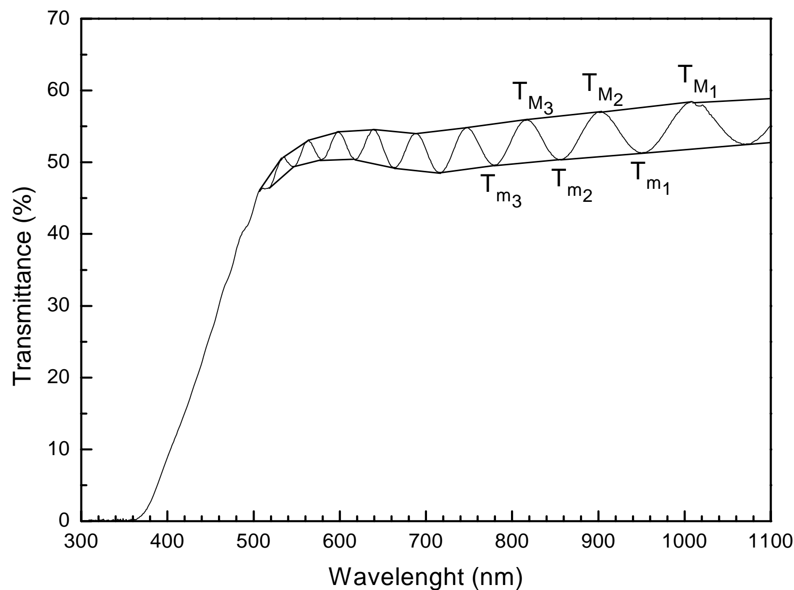

Figure 4.14 Transmittance spectrum of a Co-doped TiO_2 thin film deposited on Al_2O_3 (0001) substrate.

The transmission T for the case described in figure 4.13 is a complex function of the following variables:

$$T = T(\lambda, n_s, n, d, \alpha) \tag{4-8}$$

If n_s is known, it is convenient to write the above relation in terms of $n(\lambda)$ and the absorbance $x(\lambda)$, where $x = \exp(-\alpha d)$:

$$T = T(n, x) \tag{4-9}$$

The relation (4-8) becomes much simpler if we put $k = 0$, an approximation that is valid over most of the region of the spectrum in figure 4.14. Equation (4-9) then becomes:

$$T = \frac{Ax}{B - Cx\cos\varphi + Dx^2} \tag{4-10}$$

where: $A = 16n^2n_s$, $B = (n+1)^3(n+n_s^2)$, $C = 2(n^2-1)(n^2-n_s^2)$, $D = (n-1)^3(n-n_s^2)$, and $\varphi = 4\pi nd/\lambda$.

The extrema of the interference fringes can be written as:

$$T_M = \frac{Ax}{B - Cx + Dx^2} \tag{4-11}$$

$$T_m = \frac{Ax}{B + Cx + Dx^2} \tag{4-12}$$

For further analysis, T_M and T_m are now considered to be continuous functions of λ and thus of $n(\lambda)$ and $x(\lambda)$, as shown by the envelopes in Fig. 4.14. For any λ, T_M has a corresponding value, T_m.

We have three cases:

1) The transparent region (> 800 nm): $\alpha = 0$ or $x = 1$;
2) The region of weak and medium absorption (590 − 800 nm): $\alpha \neq 0$ or $x < 1$;
3) The region of strong absorption (<590 nm): α very large, $x \ll 1$.

In the region of weak and medium absorption the refractive index of the film is given by:

$$n = \sqrt{N + \sqrt{(N^2 - n_s^2)}} \tag{4-13}$$

where

$$N = 2n_s \frac{T_M - T_m}{T_M T_m} + \frac{n_s^2 + 1}{2} \tag{4-14}$$

and n_s, the refractive index of the substrate, is assumed to be a constant.

Practical application of this method entails, as a first step, the calculation of the maximum and minimum transmittance envelope functions $T_M(\lambda)$ and $T_m(\lambda)$, respectively. Then the refractive index is determined using the above expression (4-13).

However, for the Co-doped TiO_2 films we were unable to determine the refractive index

using this method because the amplitude of the oscillations in the transmission spectrum were not high enough and, as a consequence, the first term in the expression of N was too small: $(T_M - T_m)/T_M T_m \approx 10^{-3}$ which means that $N \approx (n_s^2 + 1)/2$. Then, it is easy to see that

$$\sqrt{N^2 - n_s^2} \approx \frac{n_s^2 - 1}{2} \quad \Rightarrow \quad N + \sqrt{N^2 - n_s^2} \approx n_s^2 \quad \Rightarrow \quad n = \sqrt{N + \sqrt{N^2 - n_s^2}} \approx n_s \qquad (4\text{-}15)$$

Therefore, we used the transmission spectra to estimate the thickness of the film, assuming that the refractive index has a variation with the wavelength as given by the following curve:

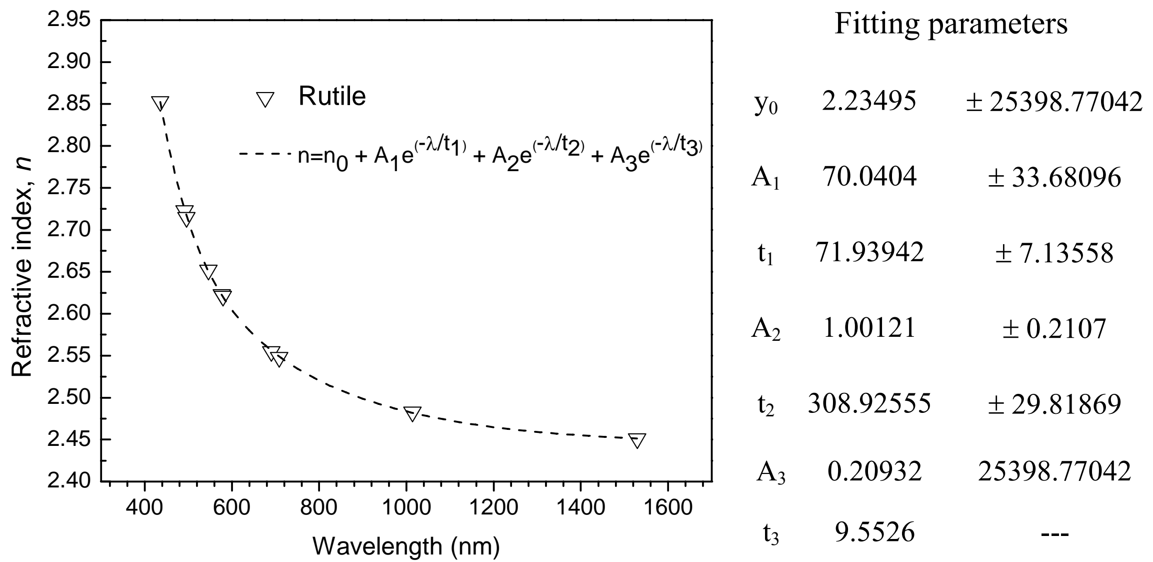

Fitting parameters

y_0	2.23495	± 25398.77042
A_1	70.0404	± 33.68096
t_1	71.93942	± 7.13558
A_2	1.00121	± 0.2107
t_2	308.92555	± 29.81869
A_3	0.20932	25398.77042
t_3	9.5526	---

Figure 4.15 Variation of the refractive index of rutile[23, 24] with the wavelength.

Film thickness

Once we know the refractive index of the film, deduced from the above curve fitting, we can determine its thickness, *d*. If $n_1(\lambda_1)$ and $n_2(\lambda_2)$ are the refractive indices at two adjacent maxima (or minima) at λ_1 and λ_2, the thickness is given by[25]:

$$d = \frac{M\lambda_1\lambda_2}{2(\lambda_1 n_2(\lambda_2) - \lambda_2 n_1(\lambda_1))} \qquad (4\text{-}16)$$

where $\lambda_1 \rangle \lambda_2$ and M is the number of oscillations between the two extrema (M=1 between two consecutive maxima or minima).

Table 4.4 shows the average value of film thickness, <*d*>, for different samples determined

by equation (4-16) using adjacent maximum and minimum and the corresponding refractive indeces deduced from the fitting curve in figure 4.15. The calculated values agree well with those determined by Rutherford Backscattering Spectrometry and Ellipsometric measurements.

Table 4.4 Values of λ_1, λ_2 , n_1, n_2 and d for some of the Co-doped TiO_2 samples.

Sample	Max. for various λ_1(nm)	Min. for various λ_2 (nm)	n_1	n_2	<d> (nm)
F93	596.582	618.317	2.39764	2.38321	
	651.972	683.172	2.36440	2.34989	1231.9
	722.787	765.907	2.33446	2.32052	
	817.090	877.388	2.30686	2.29379	
F98	608.852	648.466	2.38924	2.36619	
	702.804	765.556	2.34188	2.32063	857.7
	829.360	574.341	2.30397	2.41736	
F99	623.575	657.931	2.38008	2.36143	
	701.752	755.039	2.34229	2.32380	1007.6
	817.791	882.296	2.30669	2.29285	

Absorption coefficient

The absorption coefficient is derived from the transmission by the following relation:

$$\alpha = \frac{1}{d}\ln\left(\frac{1-R}{T}\right) \quad (4\text{-}17)$$

where d is the film thickness, T is the transmission of the film and R is its reflectance.

Using the above expression, we can plot the absorption coefficient α versus λ for the Co-doped TiO_2 thin films deposited onto Al_2O_3(0001) substrate. Three examples are shown on Fig. 4.16.

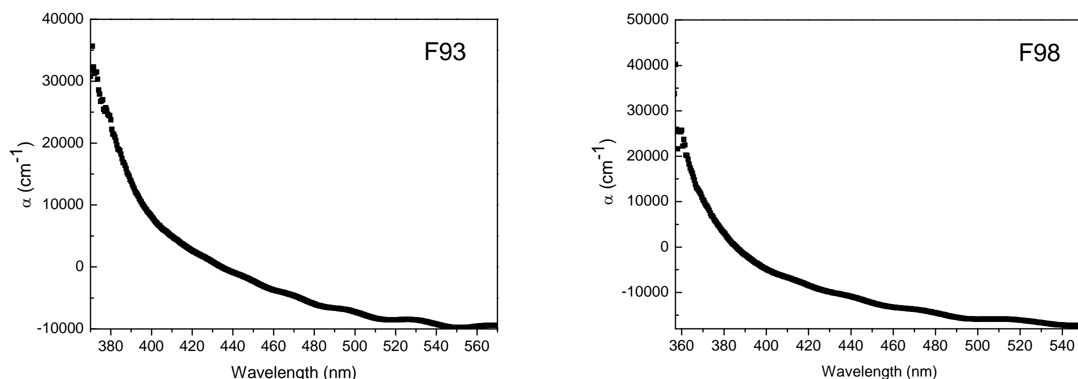

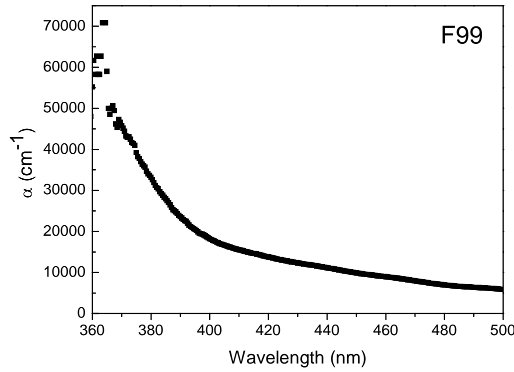

Figure 4.16 Absorption coefficient α versus λ for different Co-doped TiO_2 thin films deposited onto Al_2O_3 (0001) substrate.

Determination of the optical energy band gap of the films

Theoretical calculations have shown that for Co-doped TiO_2, which is an indirect semiconductor, α obeys the equation: $\alpha h\nu = A(h\nu - E_{gap})^2$ around the band-gap. Therefore, an obvious thing to do is to plot the quantity $(\alpha h\nu)^{1/2}$ as a function of the photon energy, hν, and fit a straight line to this plot. The intercept with the 'hν' axis will give the value of $E_{gap.}$ Figure 4.17 illustrates this procedure for the samples of Fig. 4.16.

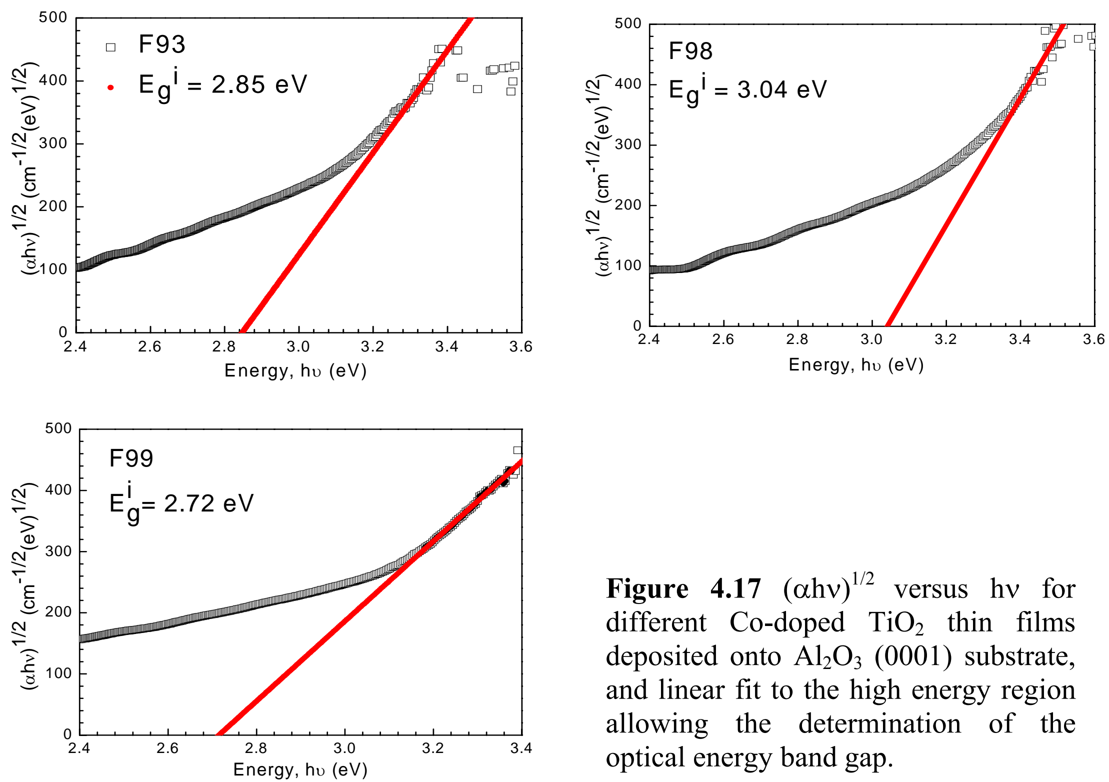

Figure 4.17 $(\alpha h\nu)^{1/2}$ versus hν for different Co-doped TiO_2 thin films deposited onto Al_2O_3 (0001) substrate, and linear fit to the high energy region allowing the determination of the optical energy band gap.

4.3.7 Resistivity measurement

Semiconductor material research and device testing often involve determining the resistivity and Hall mobility of a sample. The resistivity of a semiconductor material is primarily dependent on bulk doping. In a device, the resistivity can affect the capacitance, the series resistance, and the threshold voltage.

The electrical sheet resistance of the deposited films was determined with a linear four-point probe arrangement (Figure 4.18-a). The two contacts in the centre were connected to a voltmeter with high input impedance and the outermost contacts were connected to a current generator in series with an ammeter. For good accuracy, the diameter of the point contact tip, *lc*, should be much smaller than the tip spacing, *ls*. According to Hartnagel *et al.*[26] the electrical resistance, *R,* of a rectangularly shaped sample is given by:

$$R = \rho \times (l/bd) \qquad (4\text{-}18)$$

where ρ is the electrical resistivity of the sample and *l*, *b* and *d* are the length, the width and the thickness of the sample, respectively (see Figure 4.18-b). If *l* = *b*, equation (4-18) becomes:

$$R = \rho/d = Rs \qquad (4\text{-}19)$$

where the sheet resistance, *Rs,* is the resistance of a square of the film between opposite edges and is independent of the size of this square. For equal point contact spacing and for an infinitely thin film resting on an insulating substrate, *Rs* is given as:

$$\rho/d = Rs = (\pi/\ln 2) \times (V/I) \cong 4.53 \times (V/I) \qquad (4\text{-}20)$$

I is the measured current passing through the film and *V* is the measured voltage drop.

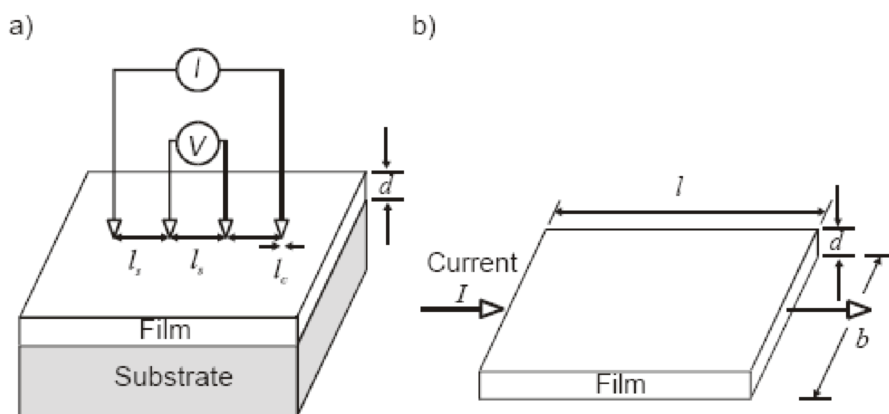

Figure 4.18 a) Four-point probe arrangement for measuring sheet resistance of a thin film; b) geometry defining the sheet resistance of a film of thickness d, length l and width b.

4.3.8 Vibrating Sample Magnetometry (VSM)

Vibrating Sample Magnetometry is based on an induction technique, which allows measuring the magnetic moment in sweeping magnetic fields, and is very effective in performing dynamic magnetic measurements. The sample under investigation is mounted at the end of a carbon fiber rod and attached to a mechanical resonator that oscillates the sample (usually in a vertical direction) at a fixed frequency in presence of external magnetizing field which is usually provided by a superconducting magnet. The superconducting magnet used for such a measurement is designed for fast sweeping rates since magnetization measurements are performed in sweeping fields. The technique involves two pick-up coils, placed above and below the sample, and the coils experience a change of the magnetic flux due to the motion of the sample. EMF voltage, proportional to the rate of change of flux, is induced in the two pick-up coils. This signal is proportional to the moment, amplitude, and frequency of vibration.

Measurements performed at cryogenic temperatures utilize low temperature cryostats or variable temperature inserts (VTI), whereas those above room temperature are possible by using high temperature oven assemblies.

4.4 References

1. J.B. Birks, "Excimers", Rep. Prog. Phys. 38 (1975) 903-974
2. D. Schuocker, “Handbook of the Eurolaser Academy”, Springer (1998), ISBN 0412819104
3. T. Ohnishi, H. Koinuma and M. Lippmaa, “Pulsed laser deposition of oxide thin films”, Appl. Surf. Sci. 252 (2006) 2466-2471
4. S.R. Foltyn, R.C. Dye, K.C. Ott, E. Peterson, K.M. Hubbard, W. Hutchinson, R.E. Muenchausen, R.C. Estler and X.D. Wu, “Target modification in the excimer laser deposition of $YBa_2Cu_3O_{7-x}$ thin films”, Appl. Phys. Lett. 59 (1991) 594
5. B. Dam, J. Rector, M.F. Chang, S. Kars, D.G. de Groot and R. Griessen, “Laser ablation threshold of $YBa_2Cu_3O_{6+x}$”, Appl. Phys. Lett. 65 (1994) 1581
6. B.D. Cullity and S.R. Stock, “Elements of X-ray Diffraction”, 3rd edition, Prentice-Hall Inc., New Jersey, 2001, p. 170
7. D5000 Diffractometer Manual - SIEMENS AG (1989)

8. Joint Committee on Powder Diffraction Standards, Powder Diffraction File, ASTM, Philadelphia, PA, 1992
9. Metal Handbook, Ninth Edition, volume 10 – “Materials Characterization”, American Society for Metals, Metals Park, Ohio (1986)
10. P.E. West, “Introduction to Atomic Force Microscopy: Theory, Practice and Applications”, Pacific Nanotechnology, 2007, www.afmuniversity.org
11. S.J. Geng, S. Zhang, H. Onishi, “XPS applications in thin films research”, Mater. Technol. 17 (2002) 234-240
12. J. Chastain (Ed), “Handbook of X-Ray Photoelectron Spectroscopy”, Minnesota, Perkin-Elmer Corporation, 1992; also, NIST tables
13. XPS Spectral Data-Base Systems & Libraries on World Wide Web URL: http//www.xpsdata.com
14. A.J. Hartmann and R.N. Lamb, “X-ray photoemission spectroscopy of thin films”, Current Opinion in Solid State & Materials Science 2(5) (1997) 511-516
15. Handbook of Modern Ion Beam Materials Analysis, edited by J.R. Tesmer and Michael Nastasi, Materials Research Society, Pittsburg, Pensylvania
16. J.M. Walls (Ed.), “Methods of surface analysis – Techniques and applications”, Cambridge University Press, Cambridge, 1989
17. L.R. Doolittle, “Algorithms for the rapid simulation of Rutherford backscattering spectra”, Nucl. Instr. and Meth. in Phys. Res. B 9 (1985) 344
18. L. Ward, “The Optical Constants of Bulk Materials and Films”, 2nd edition, Institute of Physics Publishing Ltd (1994)
19. E. Hecht and A. Azajac, “Optics”, Addison-Wesley Publishing Company (1980)
20. F.A. Jenkins and H.E. White, “Fundamentals of Optics”, McGraw-Hill International Editions, Physics Series (1981)
21. M.V. Klein and T.E. Furtak, “Optics”, John Wiley & Sons (1986)
22. R. Swanepoel, “Determination of the thickness and optical constants of amorphous silicon”, The Institute of Physics (1983)
23. http://www.moose-hill.com/rutile.htm
24. http://www.almazoptics.com/TiO2.htm
25. J. C. Manifacier, J. Gasiot, J. P. Fillard, “A simple method for the determination of the optical constants n, k and the thickness of a weakly absorbing thin film”, J. Phys. E 9 (1976) 1002
26. H.L. Hartnagel, A.L. Dawar, A.K. Jain and C. Jagadish, “Semiconducting Transparent Thin Films”, Institute of Physics Publishing, Bristol (1995)